Damage assessment and performance evaluation of self-repaired concrete specimens under constant amplitude, high-cycle fatigue

Available online at www.sciencedirect.com

ScienceDirect

Procedia Structural Integrity 47 (2023) 552–562

Structural Integrity Procedia

www.elsevier.com/locate/procedia

27th International Conference on Fracture and Structural Integrity (IGF27)

Damage assessment and performance evaluation of self-repaired concrete specimens under constant amplitude, high-cycle fatigue

G. Anglani[a], P. Marin Montanari[a], I. Iturrioz[b], P. Antonaci[a], G. Lacidogna[a]

[a]*Department of Structural, Geotechnical and Building Engineering (Politecnico di Torino); Corso Duca degli Abruzzi 24, Torino 10129, Italy*
[b]*Department of Mechanical Engineering (Universidade Federal do Rio Grande do Sul), R. Sarmento Leite 425, Porto Alegre 90050-170, Brazil*

Abstract

The study of self-healing cementitious materials has gained traction recently due to the research for more sustainable, lasting, and safer structures. The performance evaluation of such materials is usually done using static tests, with few studies involving fatigue loading. Moreover, the use of Acoustic Emission (AE) technique for damage evaluation of such structures by means of AE parameters such as the Felicity Ratio, Calm Ratio, and *b*-value seems not to have been covered to a greater extent. In this sense, the present work aims to fill this gap by using the described tools to analyze the performance and damage level of self-healing concrete specimens subjected to constant-amplitude fatigue tests involving a large number of cycles.

Keywords: Self-Healing Concrete; Fatigue Testing; *b*-value; Felicity Ratio; Calm Ratio.

1. Introduction

Due to its low tensile strength and the presence of defects from improper construction, shrinkage, or other causes, cracks in concrete are almost inevitable. Although the presence of cracks does not always increase the risk of a concrete structure collapsing, it undoubtedly affects how well it functions, speeds up its deterioration, and shortens its useful life. The study and development of intelligent self-healing cementitious materials was prompted by the growing concern for the safety and sustainability of concrete structures [1, 2]. To safely implement these novel materials in real-life constructions, the assurance of repair provided by the self-healing effect is a critical issue. For this reason, several characterization methodologies were proposed in the past decades to evaluate the effectiveness of different proposed self-healing technologies with reference to one or more material properties [3]. When studying the self-healing capabilities of construction materials, an important contribution can be achieved through the use of different

* Giuseppe Lacidogna. Tel.: +39-011-090-4871 ; fax: +39-011-090-4899.
E-mail address: giuseppe.lacidogna@polito.it

10.1016/j.prostr.2023.07.069

nondestructive testing techniques (NDT) [3, 4], whose successful examples are ultrasound [5–12] and Acoustic Emission [12–21], among others. In this study, cementitious macro-capsules embedded in a cementitious matrix were used to investigate the behavior of self-healing specimens. In addition to providing good recovery in terms of durability and mechanical resistance [22], the capsules were proven effective in assuring protection for and properly releasing a number of healing agents from the most popular types (i.e., minerals, polymers, and bacterial agents) [23]. Moreover, the cementitious capsules present inherent compatibility with the surrounding matrix and the potential to sustain the mixing process. Until now, however, most studies concerning self-healing cementitious materials involved static loading [3, 6–8, 13–15, 17–20, 24, 25]. Studies involving cyclic loading exist [23, 26–28], however, the performance and damage assessment by means of AE techniques to evaluate parameters such as Felicity Ratio, Calm Ratio, and *b*-value in such cases has not been fully developed yet. The scope of this work was to contribute to these gaps in order to help accelerate the possibility of application of self-healing systems to real-scale structures.

Nomenclature

E_{AE}	AE signals energy [mVs]
A_i	Signal amplitude [mV]
Δt_i	Signal duration [s]
W_0	"W_0" energy [J]
P	Number of data points acquired by the testing machine
δ_i	Displacement point "i" measured by the CMOD sensor placed at the mid-span of the specimen [mm]
F_i	Load point "i" measured by the testing machine [N]
G_F	Fracture energy [N/m]
s_L	Ligament area [m^2]
M_c	Completeness Magnitude [-]
N	Number of AE signals
FR	Felicity Ratio [-]
CR	Calm Ratio [-]
b	*b*-value [-]
D	Fractal dimension of the fracture surface

2. Materials and Methods

2.1. Specimen Preparation

In this work two different healing agents were used — single-component polyurethane (PU) resins produced from Minova CarboTech GmbH (Germany) labelled Carbostop U and Carbostop F. These resins cure when in contact with moisture from air or from mortars, and differ in their viscosity, foaming factor, and presence/absence of an integral catalyst — in particular, the Carbostop U resin was accelerated and highly expansive, whereas the Carbostop F resin was not accelerated and was slightly expansive [29, 30]. The resins were encapsulated in cementitious capsules to prevent any undesired polymerization before the tests. The dimensions of the capsules were 5.5 × 8 × 55 mm (inner diameter, outer diameter, length). Samples containing the capsules with the resin Carbostop U were labeled as PUC, while the ones with the resin Carbostop F were labeled as PUF. Reference samples without any capsule were also tested, and were labeled as REF. The cementitious capsules were manufactured using a polymer-modified cement paste according to previous experiences [23], and the mixing was done in accordance with [23]. An overhead stirrer (RW 20, IKA, Germany) was used for stirring, after which the fresh cement paste was rolled around an oiled bar, leading to a smooth cementitious tube with a hollow circular cross-section. The bar was then removed, and the cementitious tubes were kept for 7 days in a humid environment (T ≈ 20 °C and relative humidity (RH) ≈ 95%) prior to being exposed to air (T ≈ 20 °C, RH ≈ 50–60%). The curing process lasted 28 days. In the end of the curing period, the tubes were cut to the aforementioned length. An epoxy coating (Plastigel, API SpA, Italy) was later applied to the internal

surface of the tubes, which was mandatory to guarantee water tightness to the capsule and to avoid any premature curing of the resins with moisture present in the fresh mortar mixes. One end of the tubular capsule was sealed with a two-component epoxy plaster (Stucco K, API SpA, Italy) before being filled with the PU resin. Finally, the second end was immediately sealed with the epoxy plaster after filling, to limit the contact time of the healing agent with the surrounding atmosphere.

Regarding the specimens, they had dimensions ($40 \times 40 \times 160$ mm^3) and were produced with a standardized mortar mix composition, in agreement with EN 196-1. Portland cement (CEM II 42.5A/LL, Buzzi Unicem S.p.A., Italy), normalized sand (grading 0–2 mm, DIN EN 196-1), and tap water were used. The water to cement ratio was equal to 0.50, while the sand to cement ratio was 3. Figures 1a and 1b show the molds used for the casting. In the PUC and PUF series, one capsule containing the healing agent was fixed in the center of the mold by means of a nylon thread, at about one third in height. A notch was also created in the samples, by means of a removable plastic element inserted at the bottom of the molds. The notch width and notch height were equal to 4 mm. The specimens also had a longitudinal hole of diameter 5 mm, with the center positioned at 15 mm from the upper face, 25 mm from the lower face, as can be seen on Figures 1c, 1d and 1e. The molds were filled in two layers and each layer was compacted on a jolting table by 60 jolts. In addition, the molds were covered with plastic foils until demolding, the day after casting. Finally, the samples were cured in a humidity-saturated environment for one week.

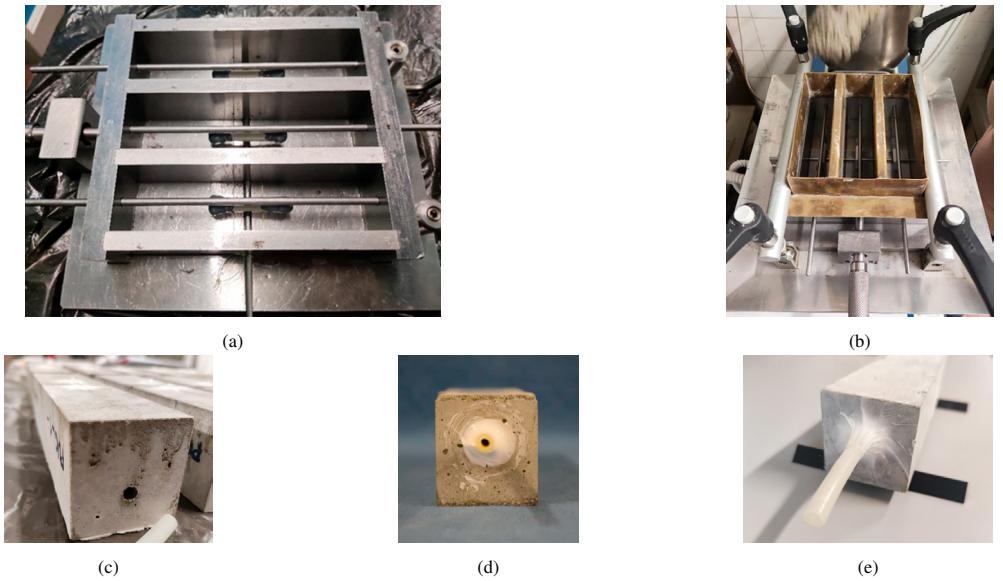

Fig. 1: Specimens preparation: molds used for casting (a,b); longitudinal hole and plastic tube used for water-flow tests (c,d,e).

2.2. Static tests

Regarding the static testing procedure, static three-point bending tests were carried out in two phases. They were conducted using a servo-controlled machine (MTS) with a maximum capacity of 250 kN and load measurement accuracy of ± 1.0%. This machine is equipped with control electronics which makes it possible to conduct tests in either load control or displacement control. All the tests were also carried out with the simultaneous acquisition of Acoustic Emission (AE) signals.

The first phase was pre-cracking tests, i.e., static tests on virgin REF, PUC, and PUF specimens, performed by Crack Mouth Opening Displacement Control (CMOD) up to a target displacement of approximately 800 microns under load. The device used for the CMOD control was a DD1 clip-on gauge manufactured by HBM, placed on the lower face of the specimen across the notch. For all tests, the specimens's mid-span deflection was also measured using the MTS piston's vertical stroke.

The second testing phase was the static reloading for the self-repaired specimens, performed under the same conditions as the first phase. Only PUCs and PUFs were subjected to the second phase because the REFs had no load-bearing

capabilities after the pre-cracking tests. It was not possible to obtain a repeatable residual crack width value for every specimen due to their different mechanical response to the pre-cracking procedure. In total, 6 REF, 8 PUC and 14 PUF (in their virgin state), 6 PUC, and 2 PUF (in their self-repaired state) were analyzed via AE, for a total of 36 samples.

Regarding the AE data acquisition, two Lunitek "AEmission" sensors were used (model LT18-003-PRD-00-R0) with a frequency range of 15–625 kHz. They were mounted on the top face of the testing specimen, vertically aligned with the supports, as can be seen on Figure 2a. The cross-section of a broken PUC specimen highlighting the capsule cross-section and the polyurethane foam partially covering the crack surface can be seen on Figure 2b. As regards the

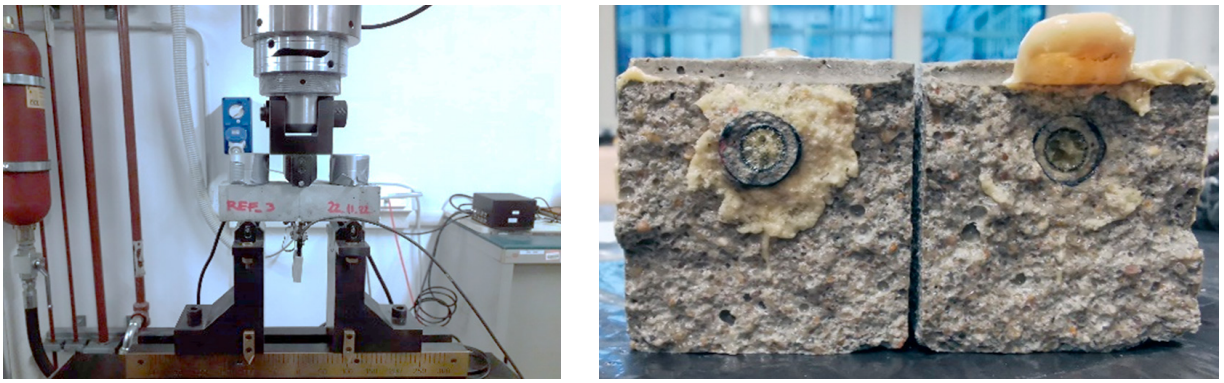

(a) (b)

Fig. 2: A REF specimen during the test with the AE sensors mounted (a) and the cross-section of a broken PUC specimen after the test (b).

creation of a longitudinal hole (Figures 1c, 1d and 1e), it is related to the setup for additional permeability analyses, that had to be performed on the same specimens by means of water-flow tests [24]. The results of these tests were not included in this paper for the sake of brevity, considering the focus on AE results. However, the detail regarding the longitudinal hole was included in the specimen description because it may have an influence on the cracking process and in the related AE analyses.

The sensors were attached to each specimen using Plasticine. The data acquisition system used a 5 MHz sampling frequency and stored data in parametric form [14]. The recorded parameters for each detected signal were:

- Signal start time: instant of the first reading that exceeds the detection threshold of 49 dB (280 μV);
- Peak amplitude, expressed in dB ($A_{dB} = 20 \log_{10} V_{\max} / V_{\text{ref}}$);
- Number of oscillations (counts): the number of intermediate crossings of the threshold by the signal. This measure is also commonly used to estimate the AE signal's average frequency (AF) through the counts/duration relationship (signal duration = start time–end time);
- AE energy (E_{AE}): integral of the waveform, as indicated by [31]. When the acquisition of the signal is parametric, it can be approximated by the envelope area of the triangle formed by the signal peak amplitude and its duration [32, 33].

The AE signals energy was calculated according to Equation 1:

$$E_{AE} = \sum_{i=1}^{N} \frac{A_i \times \Delta t_i}{2} \quad [\text{mVs}], \tag{1}$$

where A_i is the amplitude of signal "i" in mV and Δt_i is the duration of the signal "i" in s. The "W_0" energy was calculated, according to [34], as the area under the load-displacement curve, obtained via the trapezium rule, according to Equation 2:

$$W_0 = \sum_{i=2}^{P} (\delta_i - \delta_{i-1}) \left(\frac{F_i + F_{i-1}}{2} \right) \quad [\text{J}], \tag{2}$$

where δ and F are, respectively, the displacement of the piston (in mm) and the force (in N) measured by the testing machine at two consecutive data points "i" and "i-1", and P is the total number of data points acquired during the test. Examples of the load-displacement curve of virgin and self-repaired specimens are shown in the following section. The fracture energy was then calculated by dividing the "W_0" energy by the ligament area, according to Equation 3 [34]:

$$G_F = \frac{W_0}{s_L} \quad [\text{N/m}], \tag{3}$$

where W_0 is the total energy of Equation 2 in Joules [J], and s_L is the specimen's ligament area in m^2.

The specimens had dimensions $(40 \times 40 \times 160)$ mm^3 and the notch width and height were equal to 4 mm, making the ligament area equal to (40×36) mm^2, see section 2.1. The fracture energy of a virgin and a self-repaired PUC specimens can be seen in Figure 3a and 3b. The AE rate can be seen in Figure 3c and 3d for the same virgin and self-repaired specimens respectively.

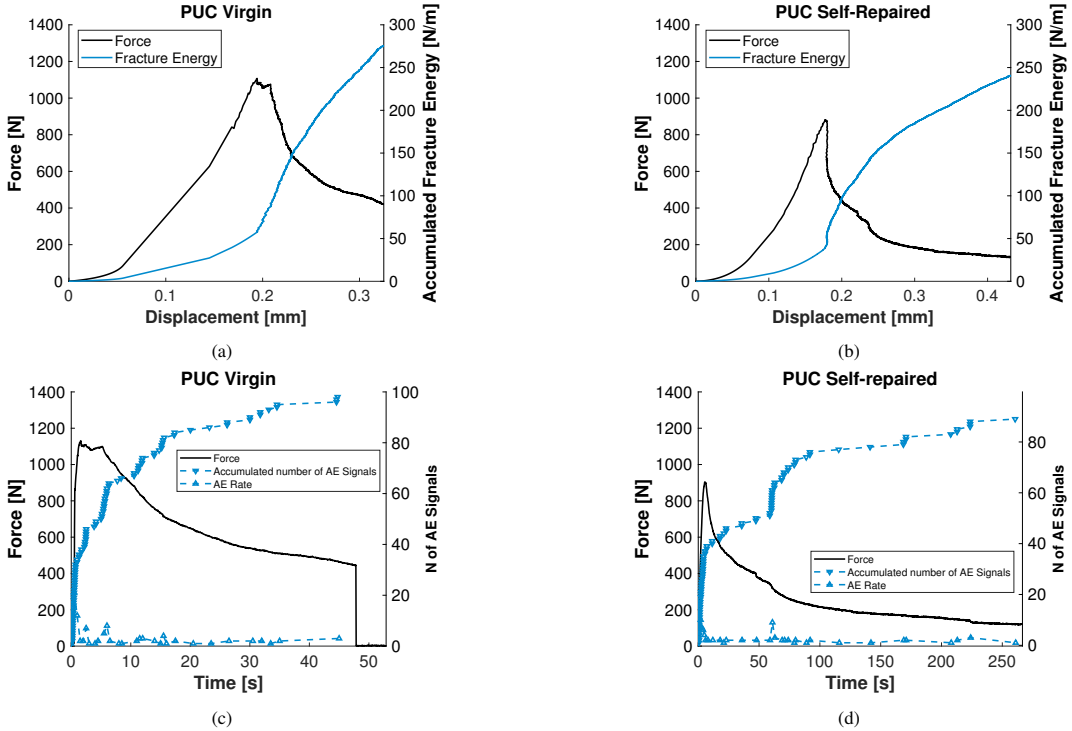

Fig. 3: Load vs displacement, load vs time, and accumulated number of AE signals vs time curves of a virgin (a,c) and a self-repaired PUC (b,d) specimen subjected to static tests.

2.3. Fatigue tests

Fatigue tests were carried out on the self-repaired specimens by submitting them to 3 Hz loading cycles of constant amplitude with loads ranging from 80 to 600 N. Every specimen was subjected initially to 1000 loading cycles and additional runs were performed with an ever-increasing number of cycles — 500, 1000, 2000, 5000, 10000, 20000, 40000, and 71500 — which lead to an accumulated number of cycles of 500, 1500, 3500, 8500, 18500, 38500, 78500, and 150000 — if failure did not occur before. The damage assessment of the fatigue tests was done by computation of the Felicity Ratio (also called Load Ratio), the Calm Ratio, and the *b*-value. As per [35], the Felicity Ratio can be calculated in the following way:

$$FR = \frac{\text{load at the onset of AE activity in the subsequent loading}}{\text{previous maximum load}},$$

and the Calm Ratio can be calculated according to [35]:

$$CR = \frac{\text{number of cumulative AE activity under unloading}}{\text{total AE activity during the whole cycle}}.$$

A scheme of a fatigue test with AE events is shown in Figure 4a. The computation of both Felicity and Calm Ratios, together, can be used to assess the level of damage of a structure, as shown in Figure 4b (adapted from [35]).

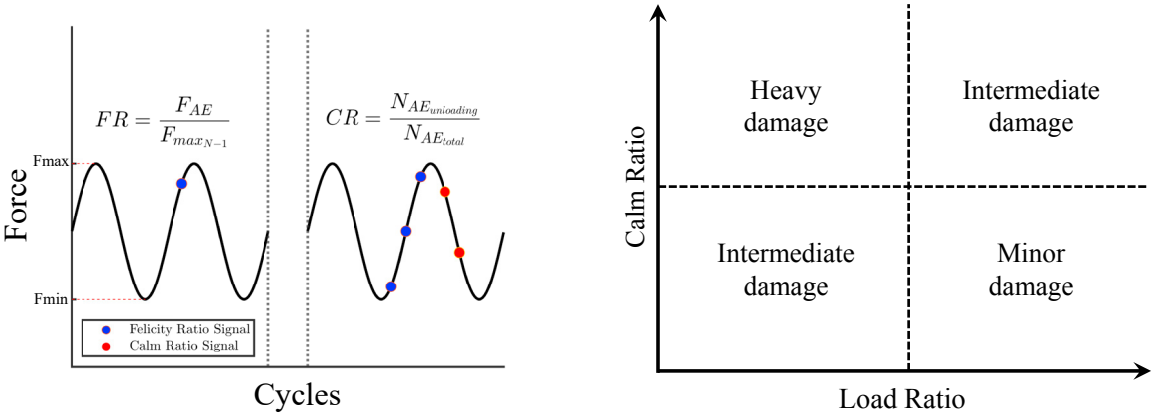

Fig. 4: Schematic of the Felicity Ratio and Calm Ratio calculations based on the AE data acquired during the fatigue test (a), and the damage assessment diagram based on these parameters reelaborated from [35] (b).

The understanding of damage evolution in time can be also significantly improved by adopting the "*b*-value" analysis procedure already used in the field of Geophysics and Earth Sciences. In this paper the *b*-value was calculated according to Equation 4:

$$\log_{10}(N \geq M) = a - b\,M, \tag{4}$$

where M is the magnitude of the AE signals, defined according to Equation 5:

$$M = \log_{10}(A/A_{\text{ref}}), \tag{5}$$

where A is the amplitude in mV, and A_{ref} is a reference amplitude (in this study, taken as 1 μV), while the b-value is defined as the negative gradient of the log-linear AE frequency-magnitude diagram and hence it represents the slope of the amplitude distribution. The b-value changes systematically with the different stages of fracture growth [32, 36], and thus it can be used to estimate the development of fracture process.

The b-value determination followed the proposal of [37]:

1. The calculation is performed step by step. A window with a certain number of AE signals is defined, as the b-value is generally not calculated using all the AE signals at once. Instead, it is normally calculated by dividing the test duration into different time windows, and by treating the windows individually;
2. For each time window, the signals are grouped based on their magnitude levels. The $\log_{10}(N \geq M)$ vs M curve is constructed by searching, for each magnitude level M, the number of signals that have an energy level greater than or equal to M, to determine the Completeness Magnitude (M_c) based on the highest-occurring frequency;
3. A linear fit of the $\log_{10}(N \geq M)$ vs M curve is performed for all the magnitude levels equal to and above the Completeness Magnitude. The negative slope of the linear fit is the b-value.

A schematic representation of the procedure can be seen in Figure 5. The temporal evolution of the b-value can be obtained by applying this methodology to every window through the test time.

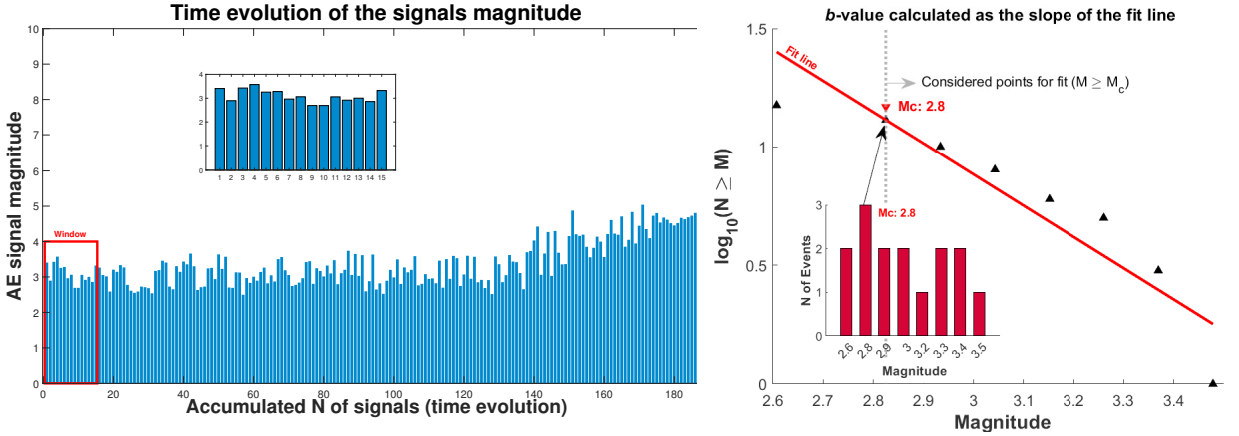

(a) (b)

Fig. 5: The three steps of the b-value calculation procedure: the subsampling of the data by the window (a); the definition of the Completeness Magnitude (subfigure) and the subsequent best fit line of the data, whose negative slope is the b-value (b).

3. Results and Discussion

3.1. Felicity Ratio and Calm Ratio

During the fatigue testing, the damage assessment was made by performing, firstly, the Felicity Ratio and the Calm Ratio analysis of both an uncollapsed and a collapsed PUC specimen, as can be seen in Figure 6a and 6b, respectively. The uncollapsed specimen completed 5000, while the collapsed specimen completed 721 loading cycles. The b-value analysis was carried out only on the collapsed specimen because, as failure did not occur in the case of the uncollapsed specimen, a meaningful interpretation would not possibly be achieved.

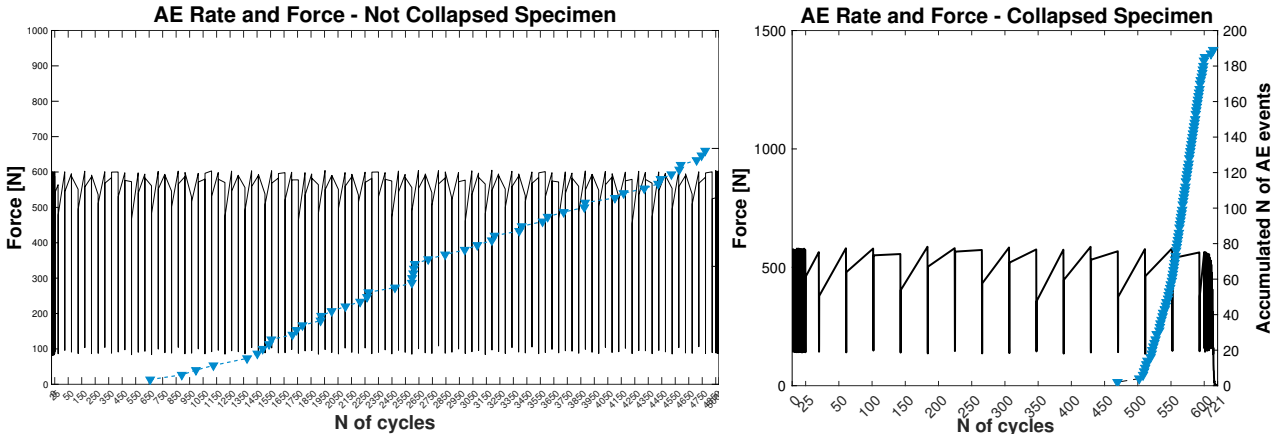

(a) (b)

Fig. 6: Load vs N of cycles curve and Accumulated N of AE events vs N of cycles curve of an uncollapsed (a) and a collapsed (b) PUC specimen.

The evolution of the Felicity Ratio can be seen in Figures 7a and 7b, and of the Calm Ratio in Figures 7c and 7d. For the uncollapsed specimen, it can be seen that both Felicity Ratio and Calm Ratio remain overall constant. Moreover, the Felicity Ratio remains high (around 0.8) and the Calm Ratio remains low (around 0.25–0.35). In the case of the collapsed specimen the situation is very different. The Felicity Ratio starts high (around 0.7) and ends very low (close to zero), while the Calm Ratio starts low (around 0.4) and finishes high (around 0.75). This is an indicator of severe damage in the specimen. The state of damage can be resumed in the damage assessment diagram, represented in Figure 8a. The values plotted are the means of the Felicity Ratio and the Calm Ratio along all cycles with AE activity. For the uncollapsed specimen, an additional static test was realized after the fatigue testing, to quantify the performance of the self-healing resin after fatigue. The load-displacement curve, as well as the fracture energy, can be seen on Figure 8b. It can be seen that the resin maintains good performance, even after the fatigue tests. The results are summarized in Table 1.

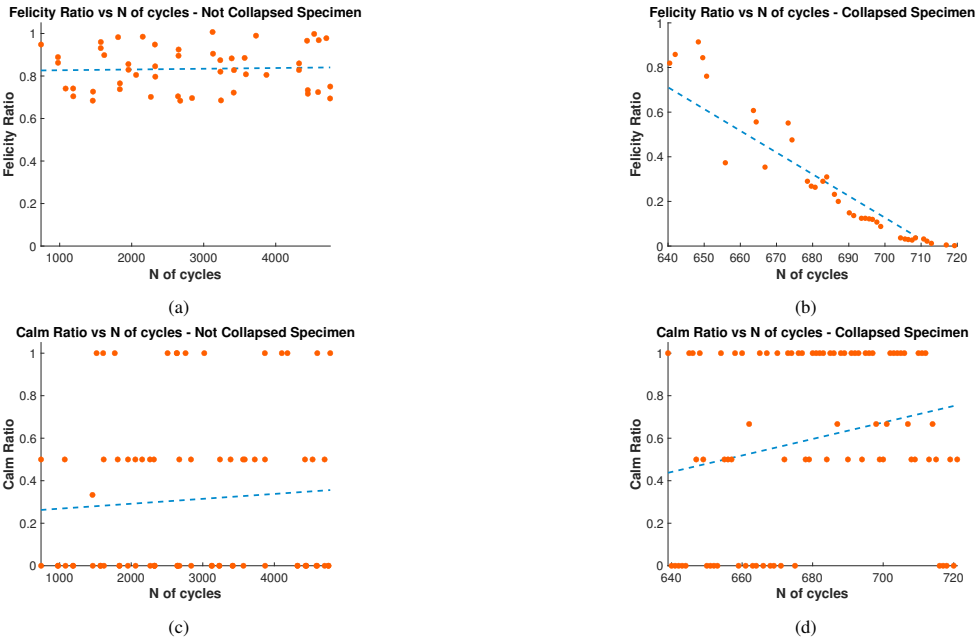

(a) (b) (c) (d)

Fig. 7: Evolution of Felicity and Calm Ratios with the N of cycles for the uncollapsed (a,c) and collapsed (b,d) specimens.

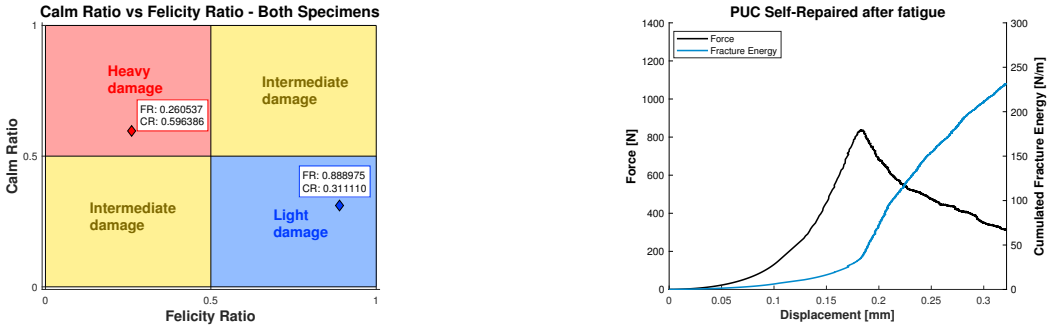

(a) (b)

Fig. 8: Damage assessment diagram for the collapsed and uncollapsed specimen (a); Load-displacement and fracture energy curves of the self-repaired specimen from a static test to evaluate the resin performance after fatigue (b).

Table 1: Comparison between PUC specimens — Virgin, Self-Repaired, and Self-Repaired after 5000 loading cycles.

Specimen	Maximum Load (*N*)	Fracture Energy (*N/m*)
PUC Virgin	1107	275.7
PUC Self-Repaired	880.7	240.7
PUC Self-Repaired after 5000 load cycles	836.1	231.3

3.2. b-value Analysis

For the case of the collapsed specimen, the 189 AE signals recorded were divided into windows containing 15 signals each, with a step of 5 signals. The *b*-value was calculated according to the procedure described in section 2.3. The *b*-value variation during the fatigue cycles can be seen in Figure 9.

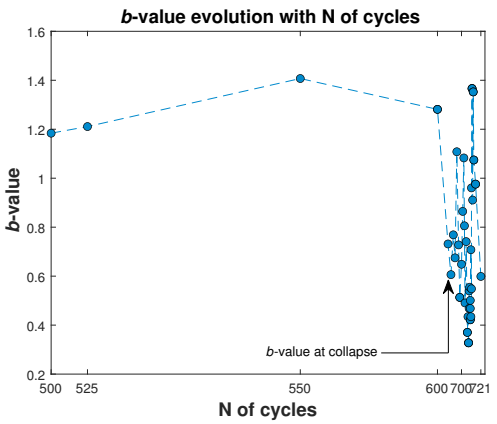

Fig. 9: Evolution of the *b*-value with the number of cycles, until collapse.

It can be observed that the *b*-value accurately indicates when catastrophic failure is about to occur as, shortly before the failure, it starts to present an erratic behavior and reaches low values (0.2–0.6). As demostrated by [36], the *b*-value is usually comprised between 1.5 and 1.0 when damage is spread over the volume of the specimen, it reaches 1.0 when the damage coalesces in the fracture surface, and it can go below 1.0 when the specimen is broken into two parts (failure). Moreover, as shown by [38], the *b*-value can be associated to the fractal dimension of the fracture

surface, according to Equation 6.

$$D = 2b. \tag{6}$$

Before the failure, as the b-value is high (1.2–1.4) the fractal dimension of the fracture is close to 3.0, which represents the process zone near the tip of the specimen notch. As failure approaches and occurs, the b-value becomes low (0.3–0.6), which is associated to a fractal dimension D close to 0.6–1.2. This represents the fact that the cracks on the body coalesce into a failure plan or edge, as expected from brittle failure.

4. Conclusions

In this work, the damage assessment of virgin and self-healed specimens subjected to static and fatigue loading was performed by computation of Fracture Energy and some parameters arising from the Acoustic Emission (AE) technique as Felicity Ratio, Calm Ratio, and b-value. Regarding the performance of the specimens, the results show that the self-healing resins retain acceptable load-bearing and fracture energy absorption capabilities when compared to the virgin specimen. Moreover, the performance loss after 5000 cycles of fatigue testing was minimal. In relation to the procedure, it was verified that the Felicity Ratio, Calm Ratio and b-value analyses as assessment tools to forecast failure can be extended to the case of high number of fatigue cycles. Specifically, the trend in the evolution of the Felicity Ratio and the Calm Ratio with the number of cycles gave insights about the upcoming failure (or not) of the specimens. In addition, the mean values of the Felicity Ratio and of the Calm Ratio throughout all cycles signed by AE signals proved to be accurate descriptors of the specimens's global behavior, as visualized on the damage assessment diagram. Finally, the evolution of the b-value with respect to the number of fatigue cycles also proved to be a good precursor of the specimen's final collapse.

Acknowledgements

The sponsorship guaranteed with basic research funds provided by Politecnico di Torino is acknowledged.

References

[1] N. De Belie, E. Gruyaert, A. Al-Tabbaa, P. Antonaci, C. Baera, D. Bajare, A. Darquennes, R. Davies, L. Ferrara, T. Jefferson, C. Litina, B. Miljevic, A. Otlewska, J. Ranogajec, M. Roig-Flores, K. Paine, P. Lukowski, P. Serna, J.-M. Tulliani, S. Vucetic, J. Wang, H. M. Jonkers, A Review of Self-Healing Concrete for Damage Management of Structures, Advanced Materials Interfaces 5 (17) (2018) 1800074.

[2] K. Van Tittelboom, N. De Belie, Self-Healing in Cementitious Materials—A Review, Materials 6 (6) (2013) 2182–2217.

[3] L. Ferrara, T. Van Mullem, M. C. Alonso, P. Antonaci, R. P. Borg, E. Cuenca, A. Jefferson, P.-L. Ng, A. Peled, M. Roig-Flores, M. Sanchez, C. Schroefl, P. Serna, D. Snoeck, J. M. Tulliani, N. De Belie, Experimental characterization of the self-healing capacity of cement based materials and its effects on the material performance: A state of the art report by COST Action SARCOS WG2, Construction and Building Materials 167 (2018) 115–142.

[4] D. Snoeck, F. Malm, V. Cnudde, C. U. Grosse, K. Van Tittelboom, Validation of Self-Healing Properties of Construction Materials through Non-destructive and Minimal Invasive Testing, Advanced Materials Interfaces 5 (17) (2018) 1800179.

[5] C.-M. Aldea, W.-J. Song, J. S. Popovics, S. P. Shah, Extent of Healing of Cracked Normal Strength Concrete, Journal of Materials in Civil Engineering 12 (1) (2000) 92–96.

[6] K. Van Tittelboom, N. De Belie, W. De Muynck, W. Verstraete, Use of bacteria to repair cracks in concrete, Cement and Concrete Research 40 (1) (2010) 157–166.

[7] L. Ferrara, V. Krelani, M. Carsana, A "fracture testing" based approach to assess crack healing of concrete with and without crystalline admixtures, Construction and Building Materials 68 (2014) 535–551.

[8] R. Alghamri, A. Kanellopoulos, A. Al-Tabbaa, Impregnation and encapsulation of lightweight aggregates for self-healing concrete, Construction and Building Materials 124 (2016) 910–921.

[9] B. Hilloulin, J.-B. Legland, E. Lys, O. Abraham, A. Loukili, F. Grondin, O. Durand, V. Tournat, Monitoring of autogenous crack healing in cementitious materials by the nonlinear modulation of ultrasonic coda waves, 3D microscopy and X-ray microtomography, Construction and Building Materials 123 (2016) 143–152.

[10] M. Ait Ouarabi, P. Antonaci, F. Boubenider, A. Gliozzi, M. Scalerandi, Ultrasonic Monitoring of the Interaction between Cement Matrix and Alkaline Silicate Solution in Self-Healing Systems, Materials 10 (1) (2017) 46.

[11] A. S. Gliozzi, M. Scalerandi, G. Anglani, P. Antonaci, L. Salini, Correlation of elastic and mechanical properties of consolidated granular media during microstructure evolution induced by damage and repair, Physical Review Materials 2 (1) (2018) 013601.
[12] G. Lefever, D. Snoeck, N. De Belie, S. Van Vlierberghe, D. Van Hemelrijck, D. G. Aggelis, The Contribution of Elastic Wave NDT to the Characterization of Modern Cementitious Media, Sensors 20 (10) (2020) 2959.
[13] K. Van Tittelboom, J. Wang, M. Araújo, D. Snoeck, E. Gruyaert, B. Debbaut, H. Derluyn, V. Cnudde, E. Tsangouri, D. Van Hemelrijck, N. De Belie, Comparison of different approaches for self-healing concrete in a large-scale lab test, Construction and Building Materials 107 (2016) 125–137.
[14] P. Minnebo, G. Thierens, G. De Valck, K. Van Tittelboom, N. De Belie, D. Van Hemelrijck, E. Tsangouri, A Novel Design of Autonomously Healed Concrete: Towards a Vascular Healing Network, Materials 10 (1) (2017) 49.
[15] E. Tsangouri, G. Karaiskos, A. Deraemaeker, D. Van Hemelrijck, D. Aggelis, Assessment of Acoustic Emission localization accuracy on damaged and healed concrete, Construction and Building Materials 129 (2016) 163–171.
[16] J. Feiteira, E. Tsangouri, E. Gruyaert, C. Lors, G. Louis, N. De Belie, Monitoring crack movement in polymer-based self-healing concrete through digital image correlation, acoustic emission analysis and SEM in-situ loading, Materials & Design 115 (2017) 238–246.
[17] K. Van Tittelboom, E. Tsangouri, D. Van Hemelrijck, N. De Belie, The efficiency of self-healing concrete using alternative manufacturing procedures and more realistic crack patterns, Cement and Concrete Composites 57 (2015) 142–152.
[18] E. Tsangouri, F. A. Gilabert, N. De Belie, D. Van Hemelrijck, X. Zhu, D. G. Aggelis, Concrete fracture toughness increase by embedding self-healing capsules using an integrated experimental approach, Construction and Building Materials 218 (2019) 424–433.
[19] E. Tsangouri, J. Lelon, P. Minnebo, H. Asaue, T. Shiotani, K. Van Tittelboom, N. De Belie, D. G. Aggelis, D. Van Hemelrijck, Feasibility study on real-scale, self-healing concrete slab by developing a smart capsules network and assessed by a plethora of advanced monitoring techniques, Construction and Building Materials 228 (2019) 116780.
[20] E. Tsangouri, D. G. Aggelis, K. Van Tittelboom, N. De Belie, D. Van Hemelrijck, Detecting the Activation of a Self-Healing Mechanism in Concrete by Acoustic Emission and Digital Image Correlation, The Scientific World Journal 2013 (2013) 1–10.
[21] K. Van Tittelboom, N. De Belie, F. Lehmann, C. U. Grosse, Acoustic emission analysis for the quantification of autonomous crack healing in concrete, Construction and Building Materials 28 (1) (2012) 333–341.
[22] G. Anglani, T. Van Mullem, X. Zhu, J. Wang, P. Antonaci, N. De Belie, J.-M. Tulliani, K. Van Tittelboom, Sealing efficiency of cement-based materials containing extruded cementitious capsules, Construction and Building Materials 251 (2020) 119039.
[23] G. Anglani, J.-M. Tulliani, P. Antonaci, Behaviour of Pre-Cracked Self-Healing Cementitious Materials under Static and Cyclic Loading, Materials 13 (5) (2020) 1149.
[24] T. Van Mullem, G. Anglani, M. Dudek, H. Vanoutrive, G. Bumanis, C. Litina, A. Kwiecień, A. Al-Tabbaa, D. Bajare, T. Stryszewska, R. Caspeele, K. Van Tittelboom, T. Jean-Marc, E. Gruyaert, P. Antonaci, N. De Belie, Addressing the need for standardization of test methods for self-healing concrete: an inter-laboratory study on concrete with macrocapsules, Science and Technology of Advanced Materials 21 (1) (2020) 661–682.
[25] A. Formia, S. Irico, F. Bertola, F. Canonico, P. Antonaci, N. M. Pugno, J.-M. Tulliani, Experimental analysis of self-healing cement-based materials incorporating extruded cementitious hollow tubes, Journal of Intelligent Material Systems and Structures 27 (19) (2016) 2633–2652.
[26] S. Cong, Z. Cheng, L. Tang, X. Ling, Fatigue properties and microstructure of graphene oxide/microcapsule self-healing concrete, Journal of Building Engineering 70 (2023) 106264.
[27] E. Cuenca, L. Ferrara, Fracture toughness parameters to assess crack healing capacity of fiber reinforced concrete under repeated cracking-healing cycles, Theoretical and Applied Fracture Mechanics 106 (2020) 102468.
[28] Y. Yang, M. D. Lepech, E.-H. Yang, V. C. Li, Autogenous healing of engineered cementitious composites under wet–dry cycles, Cement and Concrete Research 39 (5) (2009) 382–390.
[29] TECHNICAL DATA SHEET - CARBOSTOP F.
URL https://www.minovaglobal.com/media/1673/carbostop-f-tds.pdf
[30] TECHNICAL DATA SHEET - CARBOSTOP U.
URL https://www.minovaglobal.com/media/1663/carbostop-u-tds.pdf
[31] RILEM Technical Committee (Masayasu Ohtsu)**, Recommendation of RILEM TC 212-ACD: acoustic emission and related NDE techniques for crack detection and damage evaluation in concrete*: Test method for classification of active cracks in concrete structures by acoustic emission, Materials and Structures 43 (9) (2010) 1187–1189.
[32] L. Friedrich, B. Tanzi, A. Colpo, M. Sobczyk, G. Lacidogna, G. Niccolini, I. Iturrioz, Analysis of Acoustic Emission Activity during Progressive Failure in Heterogeneous Materials: Experimental and Numerical Investigation, Applied Sciences (Switzerland) 12 (8), publisher: MDPI (2022).
[33] A. Carpinteri, G. Lacidogna, M. Corrado, E. Di Battista, Cracking and crackling in concrete-like materials: A dynamic energy balance, Engineering Fracture Mechanics 155 (2016) 130–144.
[34] Determination of the fracture energy of mortar and concrete by means of three-point bend tests on notched beams, Materials and Structures 18 (4) (1985) 287–290.
[35] RILEM Technical Committee (Masayasu Ohtsu)**, Recommendation of RILEM TC 212-ACD: acoustic emission and related NDE techniques for crack detection and damage evaluation in concrete*: Test method for damage qualification of reinforced concrete beams by acoustic emission, Materials and Structures 43 (9) (2010) 1183–1186.
[36] A. Carpinteri, G. Lacidogna, G. Niccolini, S. Puzzi, Critical defect size distributions in concrete structures detected by the acoustic emission technique, Meccanica 43 (3) (2008) 349–363.
[37] Q. Han, L. Wang, J. Xu, A. Carpinteri, G. Lacidogna, A robust method to estimate the b-value of the magnitude–frequency distribution of earthquakes, Chaos, Solitons & Fractals 81 (2015) 103–110.
[38] A. Carpinteri, G. Lacidogna, S. Puzzi, From criticality to final collapse: Evolution of the “b-value” from 1.5 to 1.0, Chaos, Solitons & Fractals 41 (2) (2009) 843–853.